Effect of dual plane PIV resolution on determination of scale energy budgets in wall turbulence

N. Saikrishnan, I. Marusic, E.K. Longmire

Abstract   The dynamics of the near wall region at different scales have been analyzed recently for a Direct Numerical Simulation (DNS) of a channel flow at friction Reynolds number $Re_\tau = 180$ using a generalized form of the Kármán-Howarth equation. The present work analyzes the scale-by-scale dynamics of wall-bounded flows at higher Re_τ using data obtained from dual plane Particle Image Velocimetry experiments. Previous experiments were conducted in a zero-pressure-gradient turbulent boundary layer at $Re_\tau = 1160$, resolving scales down to 25 wall units. The results of the scale analysis were compared to DNS data of a channel flow at $Re_\tau = 934$. It was observed that the resolution of these experiments was not sufficient to capture the velocity gradients accurately enough to sufficiently determine the scale dynamics. Therefore, higher resolution dual plane PIV experiments were conducted in similar experimental conditions with a resolution of 10 wall units. The scale-by-scale energy budget obtained from this high resolution data showed a much better balance between the various terms and justified the use of higher resolution to accurately determine the velocity gradients. A simple error propagation analysis was performed to enable the choice of laser sheet separation for dual plane PIV experiments and it revealed that this parameter is a tradeoff between the truncation error of the first order approximation and the random error of the quantities measured.

1   Introduction

Wall-bounded turbulent flows have been studied using variations in physical space and in scale space. In physical space, the near wall region is classified into the viscous sub-layer, the buffer region, the logarithmic region and the outer region (Townsend, 1976). The viscous sub-layer and buffer region are the regions of largest production of turbulent kinetic energy and relatively low dissipation, implying a flux of energy towards the upper regions. The logarithmic region is an equilibrium region, where the production and dissipation match each other, with a nominally constant flux of energy transfer from close to the wall to the outer region of the boundary layer.

In the space of scales, the classical Richardson cascade was one of the earliest attempts at addressing the interaction of eddies of varying sizes. According to this theory, energy is injected into the flow at the largest scales, transferred to smaller and smaller eddies, until the energy is finally dissipated by the action of viscosity. Further, Kolmogorov (1941) stated that "in the limit of infinite Reynolds numbers, all the possible symmetries of the Navier-Stokes equation, usually broken by the mechanisms producing turbulence, are restored in a statistical sense at small scales and away from boundaries." (Monin & Yaglom, 1975; Frisch, 1995), implying the isotropy of turbulent flow at the smallest scales. Also, it was argued that in the logarithmic layer, the longitudinal energy spectrum is proportional to the wavenumber to the power $-5/3$ ($k^{-5/3}$), which was experimentally verified by Saddoughi & Veeravalli (1994). Beyond this inertial range, there is an exponential decay in energy, indicating dissipation by the action of viscosity.

N. Saikrishnan, I. Marusic, E.K. Longmire, University of Minnesota, Minneapolis, USA

Correspondence to: N. Saikrishnan, Dept. of Aerospace Engg. & Mechanics,
107 Akerman Hall, 110 Union St. SE, Minneapolis, MN 55414, USA
Email: neela@aem.umn.edu

The challenge lies in describing the scale-dependent dynamics in the presence of spatial inhomogeneities, for which a more general approach combining these two seemingly parallel ideas is required. The Kármán-Howarth equation represents an evolution equation for the longitudinal autocorrelation function and provides the basis for the Kolmogorov equation for stationary, homogeneous, isotropic turbulence. A generalized version of the Kolmogorov equation for inhomogeneous conditions was derived by Hill (2002) and this provided the framework for understanding the interaction between the various processes occurring at different regions of the boundary layer over a wide range of scales. This equation was the basis of an analysis by Marati *et al.* (2004), where the equation was appropriately simplified for a Direct Numerical Simulation (DNS) of a turbulent channel flow, and he contributions of different processes in the energy budget in a low Reynolds number flow were calculated.

The present study is an extension of this work, attempting to analyze and understand the scale dynamics occurring at larger Reynolds numbers using experimental and numerical data. The experimental data are obtained using dual plane Particle Image Velocimetry (PIV), which enables the determination of the complete velocity gradient tensor in a plane. These experiments provide an opportunity to understand the dynamics of scale energy at higher Reynolds numbers than discussed in the previous work by Marati *et al.* (2004). In this paper, section 2 will describe the experimental setup and parameters of the numerical simulation. Section 3 will discuss the specific form of the Kármán-Howarth equation for the current analysis, section 4 will discuss some results from the dual plane PIV experiments and DNS data, and section 5 will discuss conclusions and scope for future work.

2   Description of PIV & DNS datasets

The dual plane Particle Image Velocimetry (PIV) datasets were obtained from experiments conducted in a suction-type boundary layer wind tunnel. In the first set of experiments (LRPIV1 & LRPIV2), conducted by Ganapathisubramani *et al.* (2005), the smallest scale resolved was about 25 wall units. A second set of experiments (LRPIV3 & LRPIV4) was conducted at two additional wall-normal locations using the same resolution. The third set of experiments (HRPIV) resolved scales down to about 10 wall units. All measurement planes were located 3.3 m downstream of a trip wire in a zero-pressure-gradient flow, where the boundary layer thickness δ was measured to be 70.8 mm. The streamwise, wall-normal and spanwise directions are along the x, y and z axes respectively and the fluctuating velocity components along those three directions are represented as u, v and w. All quantities are normalized using wall variables, i.e. the skin friction velocity U_τ and coefficient of kinematic viscosity ν, and are denoted with a superscript $+$. The relevant experimental parameters are listed in Table 1. For the sake of understanding, the following description will discuss the LRPIV1 experiments. It must be noted that the other LRPIV and HRPIV experiments have an almost identical setup and processing technique except for the resolution, exact field of view and wall-normal locations.

The experiments conducted used a three-camera polarization-based dual plane PIV sys-

	Re_τ	y^+	y/δ	Δx^+	Δz^+	L_x/δ	L_z/δ
LRPIV1	1160	110	0.095	24.5	24.5	1.05	1.05
LRPIV2	1160	574	0.49	25.7	25.7	1.05	1.05
LRPIV3	1160	328	0.28	25.3	25.3	1.00	1.00
LRPIV4	1160	820	0.70	26.7	26.7	0.97	0.97
HRPIV	1100	100	0.091	10.0	10.0	0.46	0.46
DNS	934	110	0.12	11.4	5.7	8π	3π

Table 1: Parameters of the experimental and numerical datasets.

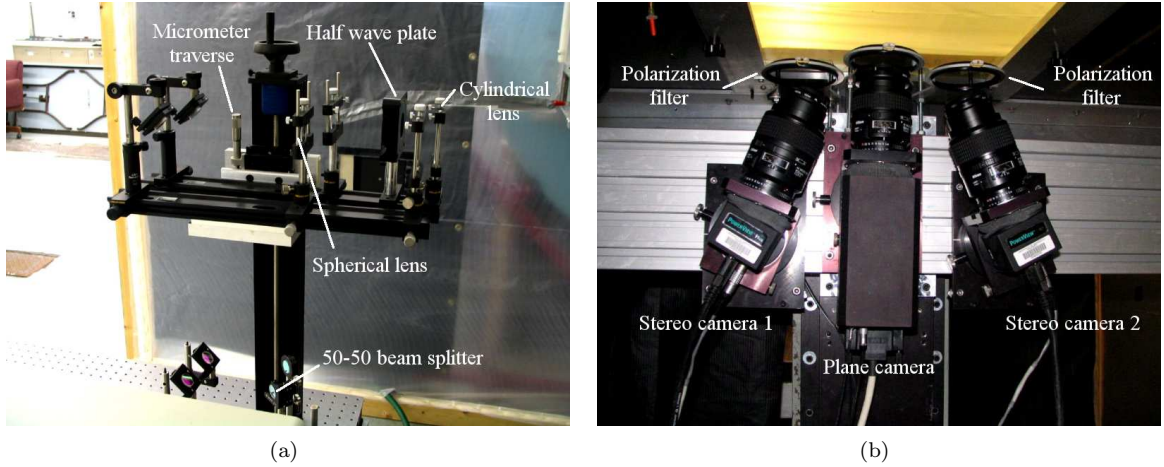(a)   (b)

Figure 1: (a) Photograph of the optical setup to generate the two light sheets. (b) Photograph of the cameras and filters.

tem as shown in Figure 1. The setup consisted of two independent PIV systems which captured images of olive oil droplets of size $\sim 1\mu$m, generated using eight Laskin nozzles upstream of the flow. The first system was a stereoscopic setup which is used to measure all three velocity components within a plane, while the second system was a conventional PIV system that measures the in-plane velocity components in a neighboring plane. Simultaneous measurements were performed in the two planes by using the polarization property of laser light sheets to isolate one camera system from the other (Kähler & Kompenhans, 2000; Ganapathisubramani *et al.*, 2005). The experiments here were conducted in the logarithmic region of the turbulent boundary layer, at a location of $y^+ = 110$.

The stereoscopic system used TSI Powerview Plus $2k \times 2k$ pixel resolution cameras with Nikon Micro-Nikkor 105 mm lenses while the second system used a Kodak Megaplus $1k \times 1k$ pixel resolution camera with a Nikon Micro-Nikkor 60 mm lens. In order to isolate the two systems from each other, the cameras were fitted with appropriate optical filters. The filters on the stereoscopic system allowed only horizontally polarized light to pass through, whereas the filters on the plane PIV system allowed only vertically polarized light to pass through. The laser sheets were generated by a Spectra-Physics

PIV-400-15 Nd:YAG laser system, pulsing about 320 mJ/pulse at 15 Hz. The beams coming out of the laser were horizontally polarized, so in order to generate two sheets of orthogonal polarization, the beams were first split into two using a CVI Laser $50 - 50$ non-polarizing beam splitter. Then, one of the beams was passed through a CVI Laser half-wave plate to rotate the polarization by $90°$. This vertically polarized beam was used to generate a sheet which was seen only by the plane PIV camera, while the horizontally polarized beam was used to generate a sheet for the stereo system. The spacing between the two sheets was adjusted using a micrometer traverse.

The vector fields for the stereoscopic cameras were obtained using the adaptive central difference technique of Wereley & Meinhart (2001) using TSI Insight 3G. To obtain the vector fields, the images obtained from PIV were interrogated using a two-frame cross-correlation algorithm with discrete window offset. Firstly, using coarse 128×128 pixel windows, the mean displacement for each window was calculated. Next, with a coarse 64×64 pixel window and the second window offset by the mean displacement, a vector field was obtained. This image was again interrogated using a 32×32 pixel window. At this step, the interrogation box in frame 1 was offset upstream and the frame 2 box was offset downstream by half the mean displacement calculated in the previous step. Thus, the final interrogation window size was 32×32 pixels and a 50% overlap was used. Due to the use of the overlap during PIV interrogation, the smallest actual scale resolved is twice the spacing of the vectors. The data from the $1k \times 1k$ cameras were also interrogated using the same method described above. In order to match the resolution between the two systems, the interrogation in this system proceeded from 64×64 pixels down to 16×16 pixels.

The vector fields were validated using a standard Gaussian engine that removed vectors with values outside 4 standard deviations from the mean. Any missing vectors were interpolated using a 3×3 local mean technique. The number of spurious vectors was close to 5% in the stereo system and about 3% in the single camera system. The data from the two planes were used to compute the entire velocity gradient tensor in the lower plane. For the in-plane gradients, a second-order central difference scheme was used, while a first-order forward differencing scheme was used to calculate the streamwise and spanwise velocity gradients in the wall-normal direction. Finally, the wall-normal gradient of the wall-normal velocity was recovered from the continuity equation. Thus the complete velocity gradient tensor was obtained using this experimental technique. The uncertainties in each quantity are discussed in detail in Ganapathisubramani *et al.* (2005).

The DNS dataset under consideration here is a numerical simulation of a fully developed channel flow. The numerical technique involves the integration of the Navier-Stokes equations in the form of evolution problems for the wall-normal vorticity and the Laplacian of the wall-normal velocity. For spatial discretization, Chebychev polynomials are used in the wall-normal direction, while de-aliased Fourier expansions are utilized in wall-parallel planes. The temporal discretization used is a third-order semi-implicit Runge-Kutta scheme. Further details of the DNS can be found in del Álamo *et al.* (2004). The simulation of interest in the present study has an $Re_\tau = 934$, which is referred to as $L950$. This

DNS dataset is used to assess the scale energy budget numerically. It must be observed that the numerical data are obtained in a channel flow, while the experimental data are obtained in a zero pressure gradient flow over a flat plate, which are fundamentally different flows in spite of the similar Re_τ. However, it is expected that for $y/\delta \leq 0.6$, the effect of the opposing wall in the channel flow should be minimal (Pope, 2000).

2.1 Choice of spacing between laser sheets

Results of an uncertainty analysis for the dual plane PIV data in Ganapathisubramani *et al.* (2005) indicated that the uncertainty in sheet separation resulted in relatively large uncertainties for $\partial U/\partial y$ and $\partial W/\partial y$. The error of approximation in the first order forward difference scheme used to determine these gradients also plays a significant role in this uncertainty. A small Δy implies a smaller error of approximation in the differencing scheme, which is particularly important near the wall where the mean velocity gradients are high. However, a very small Δy results in a high uncertainty due to the uncertainty in sheet separation. A preliminary analysis is presented below to provide an insight into the factors to be considered in choosing an optimal sheet separation. Since $\partial U/\partial y$ is the term which can be easily estimated using the mean profile of the boundary layer, this term will be used to discuss errors due to the sheet spacing.

The Taylor series approximation of the velocity at point 2 in terms of values at point 1 located at a distance of Δy is

$$U_2 = U_1 + \left(\frac{\partial U}{\partial y}\right)_1 \Delta y + \left(\frac{\partial^2 U}{\partial y^2}\right)_1 \frac{(\Delta y)^2}{2!} + \left(\frac{\partial^3 U}{\partial y^3}\right)_1 \frac{(\Delta y)^3}{3!} + \ldots$$

Rearranging the terms

$$\left(\frac{\partial U}{\partial y}\right)_1 = \frac{(U_2 - U_1)}{\Delta y} - \left[\left(\frac{\partial^2 U}{\partial y^2}\right)_1 \frac{(\Delta y)}{2!} + \left(\frac{\partial^3 U}{\partial y^3}\right)_1 \frac{(\Delta y)^2}{3!} + \ldots\right], \tag{1}$$

we obtain the first order finite difference approximation for $\partial U/\partial y$, where the sum of the terms enclosed in the square brackets is the truncation error associated with the first order finite difference approximation, with the first term being the dominant quantity. Suppose we would like to estimate the appropriate sheet separation at $y^+ = 110$. Since this point lies within the logarithmic region of the boundary layer ($y^+ > 30, y/\delta < 0.3$) The value of the second derivative of the velocity can be obtained by assuming a log profile for the velocity since this point lies within the log layer. The mean logarithmic profile is given by

$$\frac{\overline{U}}{U_\tau} = \frac{1}{\kappa} ln\left[\frac{zU_\tau}{\nu}\right] + A.$$

where $\kappa = 0.42$ is the Karman constant. Then the second derivative and corresponding error term can be written as

$$\left(\frac{\partial^2 U}{\partial y^2}\right)_1 = -\frac{U_\tau}{\kappa y^2} \qquad\qquad -\left(\frac{\partial^2 U}{\partial y^2}\right)_1 \frac{(\Delta y)}{2!} = \frac{U_\tau \Delta y}{2\kappa y^2}, \tag{2}$$

which clearly shows that smaller Δy results in smaller truncation error.

Using an uncertainty analysis similar to Ganapathisubramani *et al.* (2005), which is based on the error propagation technique of Kline & McClintock (1953), an estimate of the random error in the gradient arising from the uncertainties in the velocity and the sheet separation can be made. It can be shown that the random error in the gradient is given by

$$\delta\left(\frac{\partial U}{\partial y}\right) = \sqrt{\left(\frac{\delta U_1}{\Delta y}\right)^2 + \left(\frac{\delta U_2}{\Delta y}\right)^2 + \left(\frac{\partial U}{\partial y}\frac{\delta \Delta y}{\Delta y}\right)^2}$$
$$= \frac{1}{\Delta y}\left(\sqrt{(\delta U_1)^2 + (\delta U_2)^2 + \left(\frac{\partial U}{\partial y}\delta \Delta y\right)^2}\right), \qquad (3)$$

where δU_1 & δU_2 are the uncertainties in calculation of U in the two planes and $\delta \Delta y$ is the uncertainty in determination of the sheet separation. The above expression tells us that larger the Δy, smaller the random error.

Values documented in Ganapathisubramani (2004) are $U_\tau = 0.25$ m/s, $y = 6.6$ mm, $\delta U_1 = \delta U_2 = 0.01517$ m/s, $\delta \Delta y = 0.1$ mm and $\partial U/\partial y = 87.82$ s^{-1}, which can be used to estimate the truncation error from equation 2 and random error from equation 3. The final choice for Δy is a trade-off between these two conflicting requirements. It must be noted that while the truncation error is a definite error, the uncertainty is a possible estimate for the error, due to which the truncation error is a more stringent constraint. In other words, the truncation error generates a bias, while the random error generates an uncertainty band around the biased values. Table 2 shows the errors for different choices of y and Δy. The first row in Table 2 was used in LRPIV1 at $y^+ = 110$, while row 2 examines the possibility of reducing the sheet spacing to 0.5mm. From these two values, the choice of $\Delta y = 1.3$mm gives a small truncation error, while keeping the random error within reasonable limits. It is clear that a decrease in sheet spacing reduces the truncation error, while the random error goes up. Row 3 shows the parameters used in the HRPIV experiments, where the choice of $\Delta y = 0.5$mm is necessitated by the small in-plane resolution. This results in a low truncation error, but a high random error. At $y = 3.0$mm ($y^+ = 50$), the value of $\partial U/\partial y$ is much higher due to which the errors are higher in comparison to $y = 6.6$mm. A choice of $\Delta y = 1.3$mm results in a very high truncation error, whereas a choice of $\Delta y = 0.5$mm yields a very high random error. Hence, these errors must be kept in mind before taking a decision on the optimal spacing. The choice of spacing will mainly depend on the quantity being derived using the gradients. For example, terms involving differences of gradients between points in the same plane will lead to a cancellation of the truncation error, due to which the random error becomes more important. On the other hand, the truncation error is a more critical constraint in terms involving averages of gradients between points in the plane. A brief discussion of the possible effects of these errors on the terms of the scale energy budget will be provided in Section 4. Thus, it would be possible to come up with an estimate for the sheet separation at a given wall normal location for any experimental setup for reasonable accuracy in velocity gradients. One practical constraint which might restrict

the range of values of sheet separation is that Δy should be of the same order as Δx and Δz to remove any averaging bias in the wall-normal direction.

y (in mm)	Δy (in mm)	$\partial U/\partial y$ (in s^{-1})	Truncation error (in s^{-1})	Random error (in s^{-1})
6.6	1.3	90.2	8.9	17.9
6.6	0.5	90.2	3.4	46.5
6.0	0.5	95.2	4.0	46.9
3.0	1.3	190.5	41.3	22.1
3.0	0.5	190.5	15.9	57.4

Table 2: Estimates of truncation and random errors for various combinations of wall-normal locations and sheet spacing.

3 Equations for scale energy budget

The simplest form of the equation for the turbulent kinetic energy budget was given by Kolmogorov for homogeneous, isotropic turbulence. Before this equation is described, some definitions of various terms used in the analysis are provided. $u_i(x_i)$ represents the velocity vector at a location x_i. The velocity increment δu_i equals $u_i(x_i + r_i) - u_i(x_i)$. In some sense, $< \delta u^2 >=< \delta u_i \delta u_i >$ measures the amount of fluctuation energy contained at scale $r = \sqrt{r_i r_i}$ and hence is known as the scale energy. By a change in variables, the scale energy can be shown to be dependent on the scale r_i and the midpoint of the line joining the two points $X_{ci} = \frac{1}{2}(x_i + x_i + r_i)$. The Kolmogorov equation is given as

$$\frac{\partial < \delta u^2 \delta u_i >}{\partial r_i} = -4 < \epsilon > +2\nu \frac{\partial u^2}{\partial r_i \partial r_i}. \tag{4}$$

Hill (2002) provided a generalized form of the above equation for inhomogeneous conditions, and for a simple shear with a mean velocity U(y) in the x-direction, it reduces to

$$\frac{\partial < \delta u_j^2 \delta u_i >}{\partial r_i} + \frac{\partial < \delta u_j^2 \delta U >}{\partial r_x} + 2 < \delta u \delta v > \left(\frac{dU}{dy}\right)^* + \frac{\partial < v^* \delta u_j^2 >}{\partial Y_c}$$
$$= -4 < \epsilon^* > +2\nu \frac{\partial^2 < \delta u_j^2 >}{\partial r_i \partial r_i} - \frac{2}{\rho} \frac{\partial < \delta p \delta v >}{\partial Y_c} + \frac{\nu}{2} \frac{\partial^2 < \delta u_j^2 >}{\partial Y_c^2}, \tag{5}$$

where Y_c is the wall-normal location of interest, ϵ is the one-point pseudo-dissipation given by $\epsilon = \nu < \partial u_i/\partial x_j \partial u_i/\partial x_j >$ and * denotes a mid-point average i.e. $\epsilon^* = \frac{1}{2}(\epsilon(x_i) + \epsilon(x_i + r_i))$. In the above equation, terms with derivatives in r_i represent contributions in scale space, while terms with derivatives in Y_c are in physical space. The term containing the mean velocity gradient is the production term, while the term with ϵ is the dissipation term.

In the current analysis, it is useful to study the r-averaged form of equation 5 by integrating on two-dimensional square domains of side r in wall-parallel planes as shown in

equation 3, since this enables us to study the role of energy flow across scales at a given wall-normal location.

$$Q_r(r, Y_c) = \frac{1}{r^2} \int_0^r \int_0^r q(r_x, 0, r_z | Y_c) dr_x dr_z, \tag{6}$$

where Q and q represent a generic quantity.

Averaging in wall-parallel planes eliminates the second term on the left hand side, as $\delta U = 0$ when $r_y = 0$. The r-averaged equation can now be written in a simple form as

$$T_r + \Pi + T_c = E + D_r + P + D_c, \tag{7}$$

where each term represents the corresponding term in equation 5 and is a function of (r, Y_c). Specifically, T_r gives the inertial contribution to the scale-energy flux in r-space, Π is the production term, T_c is the inertial contribution to the spatial flux of scale-energy and is strictly associated with inhomogeneity, E is the dissipation term, D_r and D_c are the diffusive components of the flux in r-space and in geometric space, respectively, and, finally, P is an inhomogeneous contribution related to the pressure-velocity correlation.

We observe that the amount of scale energy which is effectively available at a given geometric location Y_c is provided by the local production Π plus all the terms corresponding to a spatial transfer of scale-energy towards (or from) the location considered. By considering the overall turbulent transport in the wall-normal direction, we can define an effective production $\Pi_e = \Pi + T_c - P$. Analogously, the contributions of diffusive nature can be added to form a modified dissipation rate, $E_e = E + D_r + D_c$, as the sum of the actual dissipation and the diffusive fluxes of scale-energy in physical and r-space, respectively. With these definitions, equation 7 is expressed in a more concise form as

$$T_r(r, Y_c) + \Pi_e(r, Y_c) = E_e(r, Y_c). \tag{8}$$

This expression implies that the transfer across scales plus the effective production must equal the effective dissipation. This relation will hold through the various regions of the boundary layer; however the relative importance of each term varies with the location.

This tool, applied to a low Reynolds number channel flow by Marati *et al.* (2004), has recently shown that the classical decomposition of the channel into different regions maintains a well defined meaning in the context of a scale by scale analysis also. In the buffer region, production of scale-energy is predominant and feeds the spatial flux towards adjacent zones. The log-layer is an equilibrium layer where local production and dissipation balance, meaning that it is traversed by an almost constant flux of scale energy, which does not interfere with the local dynamics. The spatial flux of scale-energy is instead crucial for the sustainment of the turbulence in the bulk region. In the space of scales, typically in the log-layer, the energy balance at smaller scales is driven by the transfer of energy, while the production becomes the dominant mechanism to balance the dissipation at larger scales. This analysis used earlier by Marati *et al.* (2004) is applied to the experimental and numerical datasets at higher Reynolds numbers. It must be observed that the dual plane PIV data do not allow us to evaluate the pressure

contribution P in Equation 7. However, according to the turbulent kinetic energy budget for a turbulent boundary layer (Pope, 2000), this contribution is expected to be negligible for $y/\delta \leq 0.6$.

4   Results and Discussion

The results of the scale-by-scale analysis are presented in Figure 2. The results for the DNS data shown in figure 2(a) show a very good agreement with equation 8. For all scales, the dashed line for E_e and the symbols for $(\Pi_e + T_r)$ overlap over the full range examined. One quantity of interest shown in figure 2(a) is the cross-over scale l_c^+, defined as the scale at which the transfer and the effective production terms become equal. Below the cross-over scale, the transfer term is the dominant term, whereas at scales larger than the cross-over scale, the production is the dominant mechanism to balance the dissipation term. This difference in the dominant mechanism could prove invaluable for numerical modeling and assumptions therein. Figures 2(b)-2(e) represent the energy budget derived from the LRPIV experiments at various locations in the boundary layer. The first observation from these plots is that as we move away from the wall, the absolute magnitudes of the various terms decrease. For example, in figure 2(b) at $y^+ = 110$, the maximum value of production goes to about 0.1, whereas even at $y^+ = 328$ in figure 2(c), the maximum value of production goes only to about 0.01. At $y^+ = 820$ ($y/\delta = 0.7$) in figure 2(e), the maximum value of production is about 0.0025, and is less than the transfer term at all scales. These trends seem to suggest that most of the production of energy occurs in the region closer to the wall, which is in accordance with what is expected in a boundary layer. The second observation, which concurs with the earlier numerical study by Marati *et al.* (2004), is that the cross-over scale increases with increasing distance from the wall, and at $y^+ = 820$, the production is always lower than the transfer term, implying the lack of a cross-over scale.

A third observation from these plots is the mismatch between the dissipation and the sum of the production and transfer terms in the LRPIV experiments (Figures 2(b)-2(e)). A previous study on low resolution dual plane PIV data and DNS data by Saikrishnan *et al.* (2006) documented that larger interrogation window sizes lead to larger attenuation of rms values, indicating the necessity for zoomed-in measurements to capture the small scale effects occurring in the boundary layer. This suggests that the terms of the energy balance are not resolved accurately at the smallest scales in the flow. Since all the curves shown are integrated in the space of scales, the contribution of the smallest scales will be present in all larger scales. Hence, it is extremely important to be able to resolve the smallest scales in the flow, and account for their contributions. The mismatch could also be caused by the uncertainty in measurement of gradients using dual plane PIV. A detailed uncertainty analysis of dual plane PIV conducted by Ganapathisubramani *et al.* (2005) showed that the wall-normal gradients have an uncertainty close to 40% of the rms value of that quantity. It is possible that this uncertainty affects the quantities which are strongly dependent on the velocity gradients, such as the dissipation and the transfer across scales. The production, which is the major contributor to the effective production term, is not expected to be affected substantially by this uncertainty since it
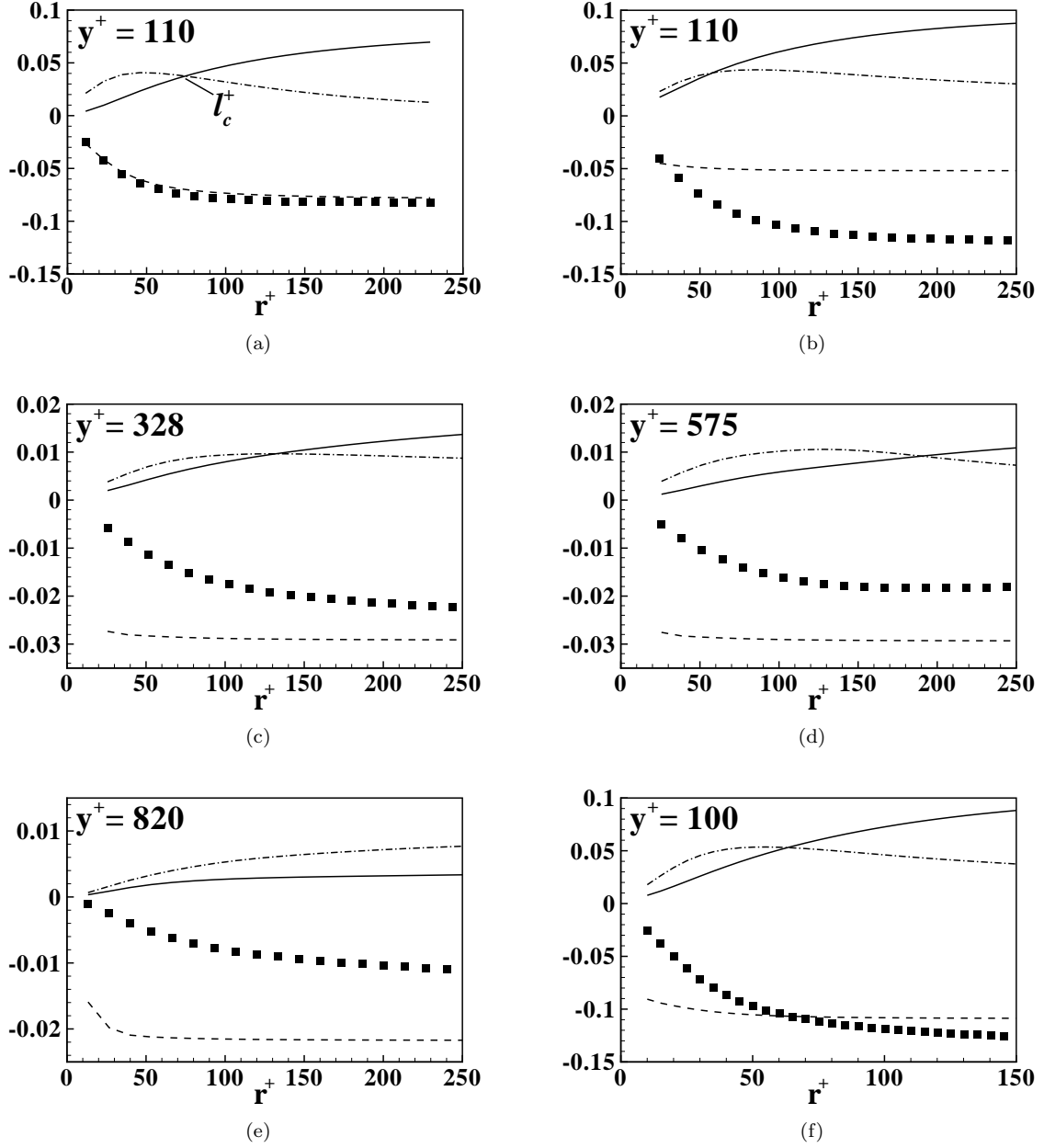
Figure 2: Detailed energy balance for (a) DNS ($y^+ = 110$) (b) LRPIV1 ($y^+ = 110$) (c) LRPIV3 ($y^+ = 328$) (d) LRPIV2 ($y^+ = 575$) (e) LRPIV4 ($y^+ = 820$) (f) HRPIV ($y^+ = 100$). The solid line is $-\Pi_e$, the dash-dotted line is $-T_r$, the dashed line is E_e and the symbols represent the sum ($\Pi_e + T_r$). All terms are normalized with wall variables ν and U_τ.
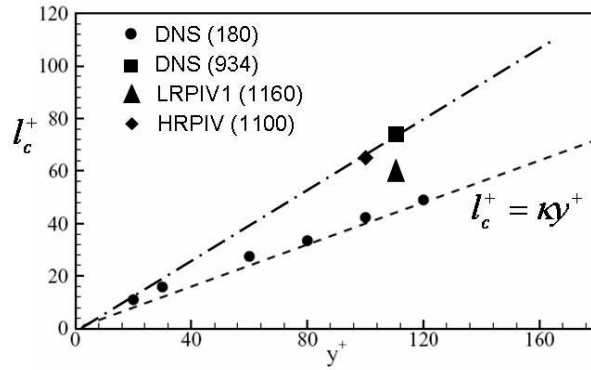
Figure 3: Plot of cross-over scale versus wall-normal location for experimental and numerical datasets (Re_τ is shown in parentheses.)

does not contain any gradients of fluctuating quantities.

The HRPIV experiments were conducted in similar conditions, but with a zoomed-in field of view, which enabled the resolution of scales down to 10.0 wall units, as shown in Table 1. The results of the HRPIV experiments shown in figure 2(f), indicate a much better balance between the dissipation and the sum of the production and transfer terms, especially at the larger scales of the flow. The mismatch towards the smaller scales could again be an effect of lack of sufficient resolution, but overall the results suggest that the high resolution experiments provide the velocity gradient quantities to much greater accuracy. With reference to the error analysis conducted in Section 2.1, from the expression for the truncation error in equation 2, it can be seen that this error is always positive. This implies that the actual value of the gradient is always larger than the approximated value. This suggests that the curve for production might be shifted to higher values. However, the transfer term would also be shifted to larger values, implying that there might not be a significant change in the cross-over scale.

The estimates of the cross-over scale obtained using the datasets at $y^+ = 110$ and $y^+ = 100$ are plotted against the values obtained by Marati *et al.* (2004) for a low Reynolds number flow in figure 3. The small circles are the data obtained in the previous study where it was observed that these data points followed a linear trend indicated by the dashed line corresponding to $l_c^+ = ky^+$. This linear relation was obtained from classical equilibrium theory in Marati *et al.* (2004). LRPIV1 gave a cross-over scale of $l_c^+ = 58$ and when the cross-over scale from the DNS $l_c^+ = 74$ and from HRPIV $l_c^+ = 66$ are plotted on this graph, they are seen to be higher than the earlier estimate as well, indicating a clear increase in this scale with Reynolds number. However, there may be be a linear trend shown by the dash-dotted line which the HRPIV and DNS datasets obey. Based on the two more trustworthy higher Reynolds number results, it is possible that the cross-over scale is a linear function of y^+, where the slope increases with increasing Re_τ. This possibility is indicated by the dash-dotted line drawn in the plot and for an approximate Re_τ of 1000, this slope is found to be 0.67. Calculation of the cross-over scale at locations closer to the wall and additional Reynolds numbers would help test this hypothesis.

5   Conclusions and future work

The balance between the various terms of the turbulent kinetic energy budget was verified for DNS and dual plane PIV data, and it was shown that high resolution PIV experiments are required to resolve the terms accurately. The results from the DNS and high resolution PIV data matched very well, both in terms of trends observed and balance of various terms verified separately. The values of the cross-over scale computed from the DNS and PIV data at higher Reynolds numbers are larger than the values predicted at a lower Reynolds number, which suggests a dependence of this value on the Reynolds number of the flow. Further experiments at different wall normal locations and higher Reynolds numbers will enable a better understanding of these trends.

The error and uncertainty analysis provided a simple method of analyzing the challenges in choosing the sheet separation for dual plane PIV experiments. The truncation and random errors are seen to be the most significant sources of uncertainty, and the tradeoff between these two conflicting errors is made depending on the appropriate quantity being calculated. The present analysis provides a starting point for a more detailed analysis of this nature to compute the parameters of the experiment.

References

del Álamo, J. C., Jiménez, J., Zandonade, P., & Moser, R. D. 2004. Scaling of the energy spectra of turbulent channels. *J. Fluid Mech.*, **500**, 135–144.

Frisch, U. 1995. *Turbulence. The legacy of A.N. Kolmogorov.* Cambridge University Press.

Ganapathisubramani, B. 2004. *Investigation of turbulent boundary layer structure using stereoscopic particle image velocimetry.* Ph.D. thesis, University of Minnesota, USA.

Ganapathisubramani, B., Longmire, E. K., Marusic, I., & Pothos, S. 2005. Dual-plane PIV technique to determine the complete velocity gradient tensor in a turbulent boundary layer. *Exp. Fluids*, **39**, 222–231.

Hill, R. J. 2002. Exact second-order structure-function relationships. *J. Fluid Mech.*, **468**, 317–326.

Kähler, C. J., & Kompenhans, J. 2000. Fundamentals of multiple plane stereo particle image velocimetry. *Exp. Fluids*, **29**(Dec.), 70–77.

Kline, S. J., & McClintock, F. A. 1953. Describing uncertainties in single-sample experiments. *Mech. Engg.*, **75**, 3–8.

Kolmogorov, A. N. 1941. The local structure of turbulence in incompressible viscous fluid for very large Reynolds numbers. *Dokl. Akad. Nauk SSSR*, **30**, 9–13.

Marati, N., Casciola, C. M., & Piva, R. 2004. Energy cascade and spatial fluxes in wall turbulence. *J. Fluid Mech.*, **521**, 191–215.

Monin, A. S., & Yaglom, A. M. 1975. *Statistical fluid mechanics: Mechanics of turbulence.* Cambridge, Mass., MIT Press, 882 p.

Pope, S. B. 2000. *Turbulent Flows.* Cambridge University Press, 806 p.

Saddoughi, S. G., & Veeravalli, S. V. 1994. Local isotropy in turbulent boundary layers at high Reynolds number. *J. Fluid Mech.*, **268**, 333–372.

Saikrishnan, N., Marusic, I., & Longmire, E. K. 2006. Assessment of dual plane PIV measurements in wall turbulence using DNS data. *Exp. Fluids*, **41**, 265–278.

Townsend, A. A. 1976. *The structure of turbulent shear flow (2nd edition).* Cambridge University Press, 438 p.

Wereley, S. T., & Meinhart, C. D. 2001. Second-order accurate particle image velocimetry. *Exp. Fluids.*, **31**, 258–268.